

# Imaging deep crustal magmatic processes in the Central Main Ethiopian Rift zone using 3-D Magnetotellurics

J. Hübert<sup>1,2</sup>, K. Whaler<sup>1</sup>, S. Fisseha<sup>3</sup>, C. Hogg<sup>4</sup>

<sup>1</sup>School of GeoSciences, University of Edinburgh, Edinburgh, UK

<sup>2</sup>British Geological Survey, Edinburgh, UK

<sup>3</sup>Institute for Geophysics, Space Science and Astronomy, Addis Ababa University, Ethiopia

<sup>4</sup>Dublin Institute for Advanced Studies, Dublin, Ireland

## Key Points:

- We collected new broadband and long period magnetotelluric data in the Central Main Ethiopian Rift
- We obtained a new three-dimensional model of electrical resistivity of the crust and uppermost mantle
- A large conductor starting at 20 km depth indicates substantial melt storage in the lower crust under the rift

---

Corresponding author: J. Hübert, [juliane.huebert@bgs.ac.uk](mailto:juliane.huebert@bgs.ac.uk)

## Abstract

In active continental rifts, asthenospheric upwelling and crustal thinning result in the ascent of melt through the crust to the surface. In the Main Ethiopian Rift (MER) most volcanic activity is located in magmatic segments in the rift center, but there are also areas of significant off-axis magmatism. Imaging the deeper parts of magmatic plumbing systems is possible with several geophysical techniques including magnetotellurics (MT). We collected MT data at 67 sites and derived a three-dimensional inversion model of the electrical conductivity in the Central Main Ethiopian Rift, testing inversion parameters and model feature robustness. High conductivity indicating the presence of melt and potential pathways in the upper crust (above 5 km depth) is found in only a few places. In contrast at mid crustal levels below 15 km depth, higher conductivity values associated with partial melt are pervasive along the north-western part of the rift. Using geochemical information to constrain melt conductivities and two-phase mixing models we estimate melt content for the middle to lower crust. We compare the conductivity model with regional shear wave tomography results. In the lower crust there are lower shear wave velocities coinciding with higher conductivities, indicating the presence of partial melt. Furthermore, there is a high velocity anomaly in the upper crust ( $\sim 5$  km depth) under Aluto volcano, where MT images a resistive body. Both observations are consistent with an older cooled magma body.

## Plain Language Summary

The East African Rift Zone is famous as the location of active continental breakup. The movement of the plates away from each other causes earthquakes and a lot of volcanic activity. To understand these geological processes, we have used the magnetotelluric method (MT) that records the natural variations in the electric and magnetic fields. MT data are good at locating molten rock in the subsurface because melt influences how easily electrical currents flow through the ground. We collected new data and built a full three-dimensional model in the Central Main Ethiopian Rift. We found that magma is likely stored close to the surface in only a few places, but that partial melt is common below 15 km depth. We compare our model with a different type of geophysical data – shear wave velocity – which describes how fast a certain variety of seismic waves generated by earthquakes travels through the rocks. We find that they agree in imaging the large-scale structure. Partial melt is being stored in the lower crust and there is an older cooled magmatic body in the upper crust.

## 1 Introduction

In active continental rifts, asthenospheric upwelling and crustal thinning are associated with lateral extension and, in the case of magma-assisted rifting, the ascent of melt from the upper mantle through the crust and even to the surface. The resulting volcanic activity can pose a hazard to local population and infrastructure that is often difficult to characterize and quantify due to data scarcity for both eruption history and the current state of the magmatic system. Imaging the deeper parts of magmatic plumbing systems is possible with only a few geophysical techniques. The magnetotelluric (MT) deep sounding method is sensitive to the presence of melt at depth as this raises the bulk conductivity of the rock. The resolution of the derived models of electrical conductivity (or its inverse, resistivity) decreases with depth but, together with petrological models obtained from the investigation of eruptive products, and seismic and gravity data, it is possible to image and quantify the melt content of the crust. Recent years have seen a shift in our understanding of magmatic systems and melt storage at deeper crustal levels, especially with the introduction of the concept of magmatic ‘mush’ (Cashman et al., 2017). This argues that melt in the crust has a very high crystal fraction and mush will therefore have different properties than melt stored in magma chambers.

In the following we present the data, processing and modelling results from new MT measurements carried out in 2016 and 2017 over a 100 km x 100 km area of the Main Central Ethiopian Rift (CMER), a volcanically active part of the East African Rift zone. We derive a 3D inversion model of electrical resistivity and use this to infer melt content at depth. We also compare our model with seismic shear waves in the area.

## 2 Geological Setting of the Central Main Ethiopian Rift

The East African Rift System (EARS) is the most prominent active intra-continental rift, extending over several thousands of kilometers. Rifting is characterized by thinning of the lithosphere and extension between the Nubian (African) and Somalian plates that is accommodated both seismically along border faults and magmatically in active volcanism (Ebinger & Casey, 2001; Chorowicz, 2005). The generation of magmas in the EARS is due to either melting within the lithospheric mantle arising from temperature fluctuations, or decompression melting of the convecting upper mantle caused by thinning of the plate during extension (Rooney, 2020). The narrow Main Ethiopian Rift (MER, see Fig. 1) separates the Ethiopian and Somalian plateaus, most of which are covered with Eocene to recent flood basalts, and forms a link between advanced rifting in the Afar depression in the north and the less developed Kenyan Rift to the south (Ebinger & Casey, 2001; Woldegabriel et al., 1990; Mazzarini et al., 2013). The MER is assumed to overlie hot and weak continental lithosphere (Keranen et al., 2009). In its middle part, the Central Main Ethiopian Rift (CMER), the extensional strain is accommodated in two Quaternary magmatic-tectonic systems, the central rift Wonji-fault belt (WJB) and the Silti Debre Zeyt fault zone (SDZF) along the western margin. The border faults are long (>50 km), and have a large offset (typically >500 m) giving rise to major escarpments separating the rift floor from the surrounding plateaus. The extension rate is about 4–6 mm/yr (Agostini et al., 2011; Keir et al., 2006; Corti et al., 2018).

The CMER is filled by late Miocene to recent volcanic rocks and continental sedimentary deposits (Corti, 2009). Exposed volcanic products consist of basalts, rhyolites, ignimbrites, and pyroclastic deposits (Fontijn et al., 2018). Monogenetic volcanic activity (spatter cones, scoria cones, maars, and lava domes) (Rooney et al., 2007; Corti, 2009; Rooney, 2010; Mazzarini et al., 2013) is widespread on the rift axis as well as along the rift margins (Rooney, 2010), with some variation along strike reflecting the increase in magma-assisted rifting towards the north (Fig. 2). From recent seismic data, the crustal thickness along the CMER has been determined to be about 35–40 km (Keranen et al., 2009; Stuart et al., 2006; Maguire et al., 2006; Keranen & Klemperer, 2008). In the northern part of the CMER, the rift structure is asymmetric, probably due to lithospheric-scale pre-existing heterogeneities (Bastow et al., 2008; Cornwell et al., 2010; Keranen et al., 2009; Corti et al., 2018), with western off-axis Quaternary magmatism in the SDZF and on-axis Quaternary tectono-magmatic activity in the WFB accommodating the current deformation. Further south both margins are dominated by large boundary faults resulting in a more symmetric architecture (Agostini et al., 2011; Corti et al., 2018).

Seismicity in the CMER has been observed in the EAGLE (rift-wide), ARGOS (local installation on Aluto volcano) and Bora-Tulu Moye (see Fig. 2) experiments (Keir et al., 2006; Wilks et al., 2017; Greenfield et al., 2019b). The larger earthquakes in the catalogues are related to movement on the border faults (see cyan circles in Fig. 2), whereas under the volcanoes, most events of lower magnitude ( $M_W < 3$ ) are observed in the shallower regions of the hydrothermal systems with a fewer deeper (5 km) events related to magma storage (Greenfield et al., 2019a). In general, the CMER is seismically quieter than the Northern MER (NMER). This is associated with the wider presence of partial melt and heating of the upper crust in the CMER, whereas in the NMER deep crustal seismicity can be explained by the propagation of faults in the strong and brittle crust (Lavayssiere et al., 2018), although some earthquakes there are induced by magmatic pro-

cesses (Keir et al., 2009). In the CMER, the deformation from rifting is now thought to be mostly accommodated in the magmatic segments.

### 3 New Magnetotelluric Data

MT data presented and analysed in this study were collected during two field campaigns and comprise the rift-crossing profile data with 26 sites from 2016 (described by Hübner et al. (2018)) and a further 37 sites in an 100 x 100 km array covering the CMER collected in 2017. Data acquired in the March-May 2017 survey include 12 long period sites (LMT) and 25 additional broadband recordings (BMT).

During both campaigns, broadband MT and long-period MT data were collected. At all sites, the horizontal electric field variations were recorded ( $E_x$  for north-south and  $E_y$  for east-west), using non-polarizable electrodes, in addition to the three components of the magnetic field ( $H_x$  is the north-south,  $H_y$  the east-west and  $H_z$  the vertical component). Broadband MT sites recorded the field variations with Phoenix MTU5A systems using induction coils. LMT data were collected with Lemi-417 instruments and flux-gate magnetometers. LMT sites were first occupied over 1-3 days by a broadband system and then for 2-3 weeks by a Lemi-417 instrument. Site access was very difficult in the Eastern parts of the area, with just a few sites occupied in 2016. To increase data coverage we include two sites from Reykjavik Geothermal's Tulu Moye prospect in our analysis. These are good quality broadband four-channel ( $E_x$ ,  $E_y$ ,  $H_x$ ,  $H_y$ ) recordings. The site distribution is shown in Fig. 2. Sites lie approximately on 5 profiles perpendicular to the rift axis, delineated in Fig. 4. The instruments during our campaign suffered from both extreme heat and rain. Due to the dense population of the area and human interest in the measurements, data quality is somewhat mixed, ranging from very good to quite noisy. Using remote processing techniques and robust processing schemes from both Egbert (1997) and Smirnov (2003) we obtained the complex and frequency dependent transfer functions of MT, the impedance tensor  $\mathbf{Z}$ :

$$\mathbf{E}(\omega) = \begin{pmatrix} Z_{xx} & Z_{xy} \\ Z_{yx} & Z_{yy} \end{pmatrix}(\omega) \cdot \mathbf{H}(\omega)$$

and tipper

$$H_z(\omega) = \begin{pmatrix} T_{zx} & T_{zy} \end{pmatrix}(\omega) \begin{pmatrix} H_x \\ H_y \end{pmatrix}(\omega)$$

in the range of 0.01 Hz - 1,000 s for the BMT and up to 10,000 s for the LMT sites. For 3-D inversion, we selected 43 sites with good quality data and also omitted some sites from the more densely sampled across-rift profile (profile 3 in Fig. 4), that has previously been interpreted with a 2D inversion model by Hübner et al. (2018). MT data represented as phase tensors (Caldwell et al., 2004) and induction vectors (Wiese, 1962) are displayed in Fig. 3 at the sites included in the 3-D inversion. The phase tensor representation allows a quick assessment of the dimensional complexity of the underlying conductivity structure. Whereas a 2-D inversion approach could be justified along the trans-rift profile of Hübner et al. (2018), increased ellipticity and skew values over most of the period range in the southern and northern parts of the area indicate that only 3-D inverse modelling will result in a model that sufficiently explains all these data. The tippers for the shorter periods ( $T < 45$  s) are very small for most sites across the area and are therefore also more susceptible to artificial noise. Such small values can indicate a lack of lateral resistivity variations or would also be exhibited by sites overlying a conductive feature. Tippers for longer periods ( $T > 1000$  s) displayed as induction arrows have a very consistent trend pointing away from a deep conductive feature in the west (Fig. 3). The existence of this feature was previously inferred by Samrock et al. (2015) based on tippers from Aluto volcano and also modelled in the 2-D inversion by Hübner et al. (2018), approximately 50 km to its north-west.

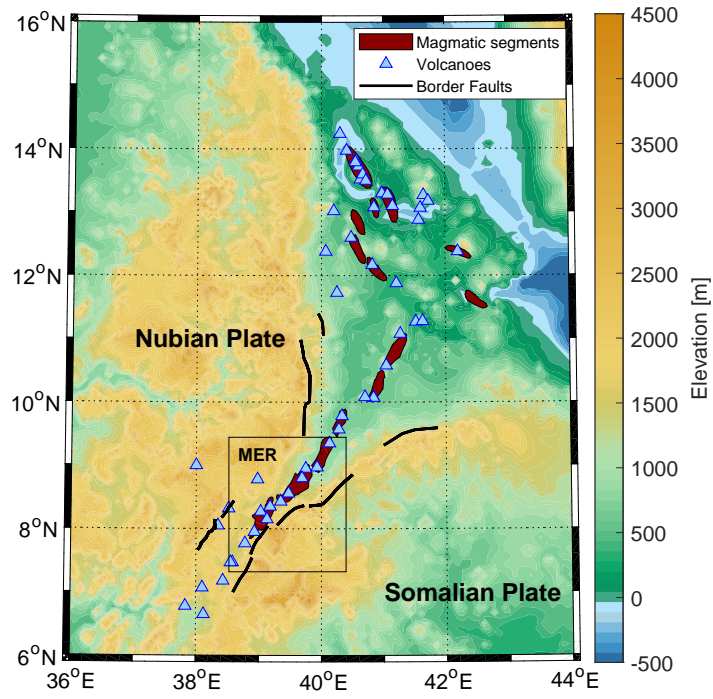


**Figure 1.** Topographical map of the northern portion of the EARS showing Quaternary magmatic segments, volcanoes and border faults. The black box is the area shown in Figure 2.

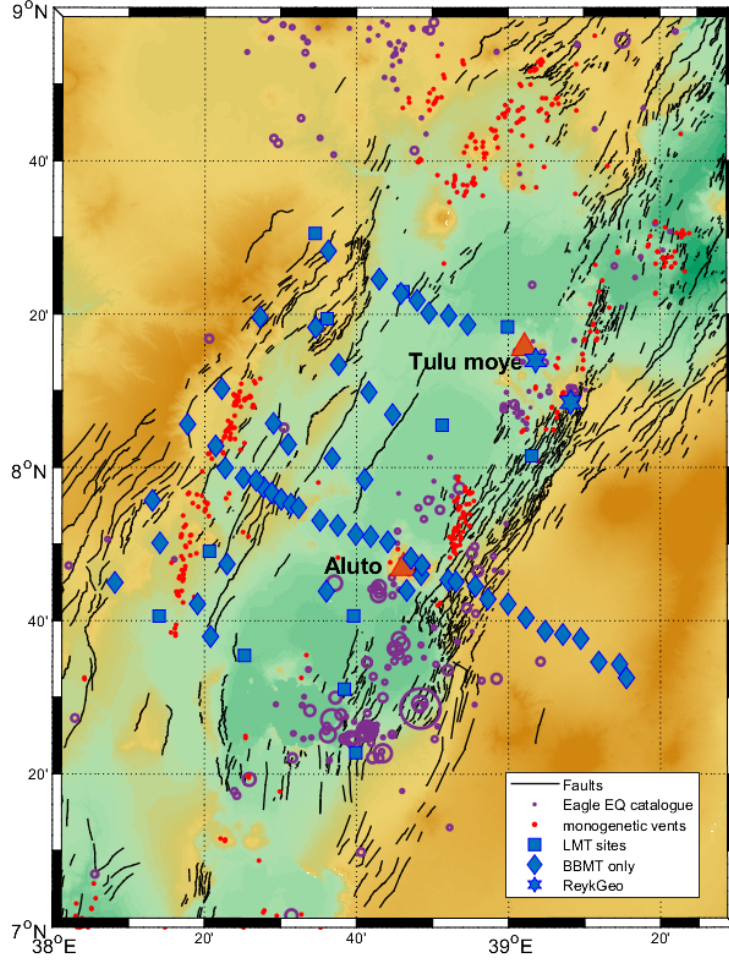


**Figure 2.** Map of the survey area in the CMER lakes region with the location of MT stations (diamonds - broadband only, squares - LMT and broadband, stars - broadband from Tulu Moye prospect, kindly provided by Reykjavik Geothermal). Black lines - faults after Agostini et al. (2011); red dots - monogenetic volcanic vents after Mazzarini et al. (2013); purple circles - seismicity with circle size proportional to magnitude (Maguire et al., 2006). Site names can be seen on the map in the supplementary material

Plots of the data used in the 3-D inversion and the respective data fit of the preferred model can be found in the supplementary material.

## 4 3-D Model of Electrical Conductivity of the CMER

### 4.1 Inverse modelling

To derive a three dimensional model of electrical resistivity in the CMER we used ModEM (Kelbert et al., 2014), a powerful parallelized data space inversion code. The model volume is 450 x 450 x 350 km, represented by 78 x 68 x 38 cells (x, y, z) whose resistivities are the model parameters. The horizontal cell dimension (north-south or latitude, east-west or longitude) is 2 km, vertically (z) it starts at 10 m and then increases logarithmically with depth. We attempted to incorporate topography into the model mesh, but the forward solution showed poor convergence. This is because most of the topography lies outside the observation area, i.e. almost all stations are within the rift, whereas there are large topographic changes between the rift and the plateaux and on the plateaux on both sides of the rift (see Fig. 2). Thus in order to facilitate convergence and keep model sizes computationally manageable a flat surface was assumed.

We investigated values of various parameters of the ModEM algorithm and inversion strategies, with some guidance from Robertson et al. (2020). We tested inverting different parts of the data (impedances, tippers, long period only and all periods), error floors (5 and 10 % for the impedance, 0.01 and 0.02 for the tipper) and covariances (smoothness of the model, from 0.1 to 0.7) as well as the regularization parameter which balances the data fit and model smoothness ( $\lambda = 1, 10, 100, 1000$  as the starting value). We tested several homogeneous starting model resistivities (10, 100 and 1000  $\Omega\text{m}$ ), but found that the logarithmic average of all data apparent resistivities, 25  $\Omega\text{m}$ , led to the best data fit. As error floor we chose 5 % of the off-diagonal impedances (setting  $\delta Z_{xx}$  to  $\delta Z_{xy}$  and  $\delta Z_{yy}$  to  $\delta Z_{yx}$ ) and 0.02 for the tippers. The covariances used for the preferred model are 0.4 and the starting  $\lambda$  is 100. We started the inversion process with the full impedance tensor data at periods greater than 1 s, and then included the shorter period data and finally the long-period tippers. Adding the long-period tippers helped constrain the presence of the deep conductive feature hypothesized by Samrock et al. (2015) and imaged by Hübert et al. (2018). The final RMS misfit is 2.9 (2.6 for the impedance data and 3.2 for the tippers, see supplementary figures).

### 4.2 Preferred 3-D model

Depth slices through the preferred model are shown in Figure 4 together with the site locations and the position of the boundary faults (black lines). The shallow part of the model (up to 2 km depth) is mostly characterized by low resistivities (below 10  $\Omega\text{m}$ ). Below 1 km depth, several more resistive features ( $>100 \Omega\text{m}$ ) are imaged. Most notably there are higher resistivities under Aluto volcano down to  $\sim 7$  km depth, along the entire SW border of the rift valley down to  $\sim 10$  km, at the SE rift flank and across the rift along the northern-most profile (profile 1) down to 3-5 km. The Tulu Moye volcanic centre in the NE corner of the model area is clearly imaged as a conductor above 2 km depth as reported in the high resolution study of Samrock et al. (2018). There is a strong conductive feature in the center of the rift between profiles 1 and 2, that at 9 km depth connects with the smaller conductor below Tulu Moye. Resistive features are only present in the upper-most 10 km of the model. Below 15 km depth, the dominant features are conductive regions in the centre north of the CMER and SW end of the survey array. These connect at around 18 km depth into one large conductive zone. Notably, the north-western rift boundary fault coincides with the lateral extent of the conductor, whereas in the south-east the conductor vanishes before reaching the rift shoulder. The deepest two sections shown in Figure 4 are in the mantle, but there is limited sensitivity to struc-

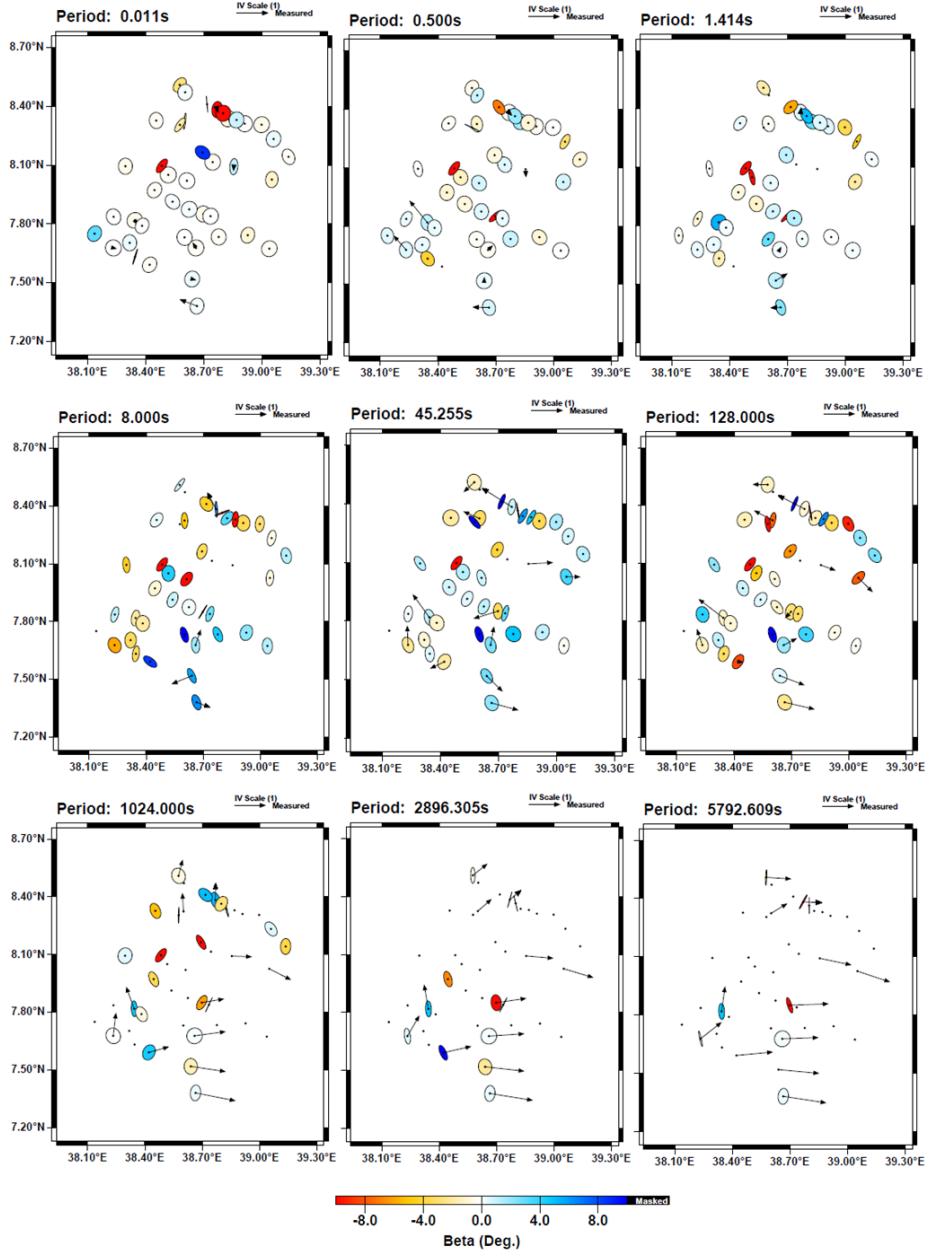


**Figure 3.** Magnetotelluric data selected for 3-D inversion as a function of period, indicated above each panel. Impedance data at both BMT and LMT sites are represented as phase tensors, after Caldwell et al. (2004). The real part of the tippers at LMT sites are displayed as induction arrows, after Wiese (1962). The fill of the phase tensors is the skew angle  $\beta$ ; the unit length for the induction arrows is 0.2.

ture at these depths. Features in the lower crust persist, but this may be a result of regularization.

### 4.3 Robustness Assessment of Conductive Features

Our preferred model did not reach the target RMS misfit of 1 mainly due to varying level of noise contamination and computational limits when choosing the grid size. It is therefore necessary to assess the robustness of some of the model parts to be able to interpret them confidently in terms of magma storage. Specifically, the extent and connection of the conductive model features were scrutinized. We tested the sensitivity of the data to certain model features by using locally perturbed models. The preferred model was modified (see Fig. 5) and the RMS misfit value (see Table 1) was calculated for the impedance response data at selected sites. Modifications to the preferred model are as follows.

1. Data coverage beyond the rift on the NW shoulder is limited, therefore we investigated the lateral extension of the deep conductor past the location of the border faults (black lines in Fig. 2). For the modified model we reduced the resistivity in cells NW of the border fault to  $5 \Omega\text{m}$  between 20 and 25 km depth. The overall data misfit value does not change, but for sites located on and close to the modified model areas there is an increase in RMS misfit, signifying that the data are sensitive to the lateral boundary of the deep conductor.
2. To test the sensitivity of the data in regards to the depth extent of the deep conductor we replaced the resistivity of all model cells below 26 km with the background resistivity of  $25 \Omega\text{m}$ . The overall RMS increases slightly from 2.60 to 2.64. Table 1 lists the consistently higher RMS values at a few sites individually.
3. Thirdly, we replaced the resistivity in the cells connecting the shallow conductor (5-15 km depth) under Tulu Moye and the deep conductor with the background resistivity value of  $25 \Omega\text{m}$ . An increase in RMS misfit is only observed for site MOY60, but it is substantial and hence demonstrates that the data require a laterally continuous conductor.

Additionally, we restarted the 3-D inversion using each of the modified models as the prior model. In all three cases the inversion changes the modified model cells and the final model resembles the preferred model (not shown). Therefore we are confident that the western boundary fault marks the north-western edge of the deep conductor, that this deep conductor extends to below 25 km, and that there is a connection between the Tulu Moye conductor and the deeper conductive region. In a final test with perturbed model parameters (not shown), the deep conductor (below 15 km) was replaced by distinct smaller ( $10 \times 10 \times 5 \text{ km}$ ) blocks of high conductivity. The resulted forward responses only very slightly differed from those of the preferred model. We therefore conclude that lateral resolution at these depths is severely limited and could only be improved with more high-quality long-period data, which are very difficult to obtain in the area.

### 4.4 Comparison of Electrical Conductivities in 2-D and 3-D Models

Including the array data and performing a 3-D inversion expands (but does not contradict) the 2-D analysis of Hübner et al. (2018). The geographic extent of the deep conductor is resolved in the 3-D model, and the upper to mid-crustal resistors in the central CMER (below Aluto and ca. 10 km north-west under the Gardemotta caldera, see Fig. 4 c-e)) are captured in both models. The main difference between the 3-D and 2-D models are the slightly smaller resistivity variations in the 3-D model. The conductor at depth had values of  $< 3 \Omega\text{m}$  (2-D) vs.  $< 10 \Omega\text{m}$  (3-D) and the mid-crustal resistors  $> 300 \Omega\text{m}$  (2-D) vs.  $> 200 \Omega\text{m}$  (3-D), resulting in smaller resistivity differences between conductive and resistive features. This is a known effect of the increased num-

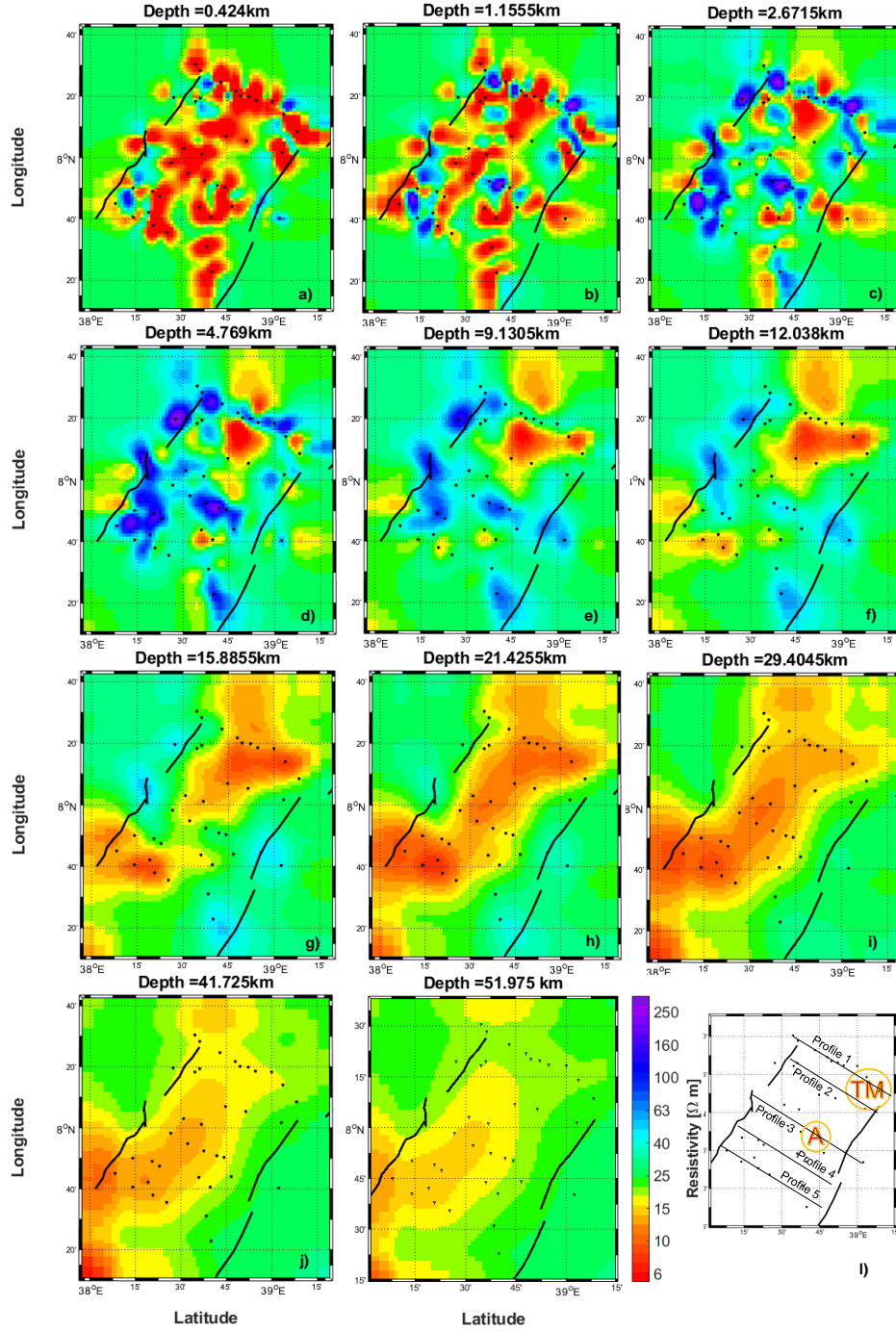


**Figure 4.** a)-k) Depth slices through the preferred 3-D inversion model. Black lines are the border faults, black dots are the location of the MT sites. Green colours match the 25  $\Omega$ m of the homogeneous starting model. Panel l) shows the location of Aluto volcano and the Tulu Moye geothermal prospect, indicated with 'A' and 'TM' respectively, and indicates the numbered profile lines referred to in the text.

**Table 1.** RMS misfit values for impedance data at selected sites for preferred and modified models. Pref - preferred model; see Fig. 4. Test1 - Extended deep conductor to beyond the western boundary fault. Test2 - Limited depth extent of conductor to above 25 km. Test3 - removed the connection between conductor under Tulu Moye and deeper conductor. Location of sites indicated in Fig. 5; RV094 and MOY060 are BMT, the others are LMT.

Site name	RMS pref	RMS test1	RMS test2	RMS test3
All	2.60	2.60	2.64	2.61
LMT001	1.30	1.60	1.30	1.30
LMT101	1.58	1.62	1.59	1.58
RV094	1.15	1.22	1.23	1.15
LMT104	1.59	1.57	1.74	1.59
LMT110	2.43	2.39	2.50	2.42
MOY060	2.15	2.15	2.20	2.33

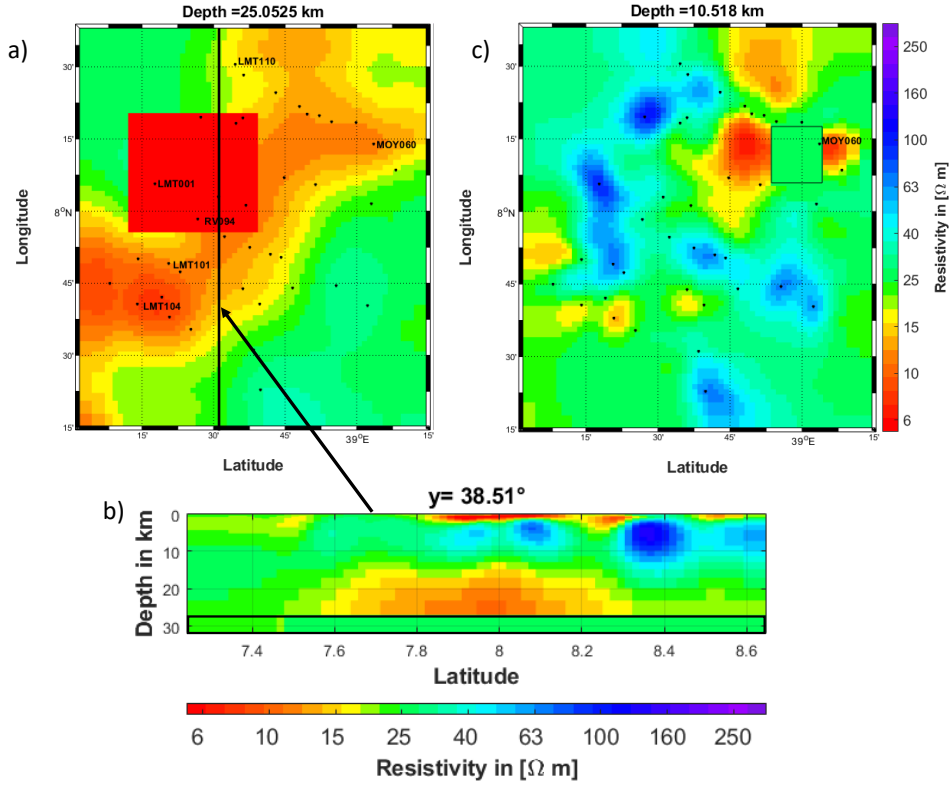


**Figure 5.** Perturbation of preferred model: a) Extended lateral boundary of the deep conductor to the NW (map view). b) Set the lower boundary of the conductor to 25 km depth (vertical section with position indicated on map in a)). c) Disconnect the deep conductor from conductor under Tulu Moye (map view).

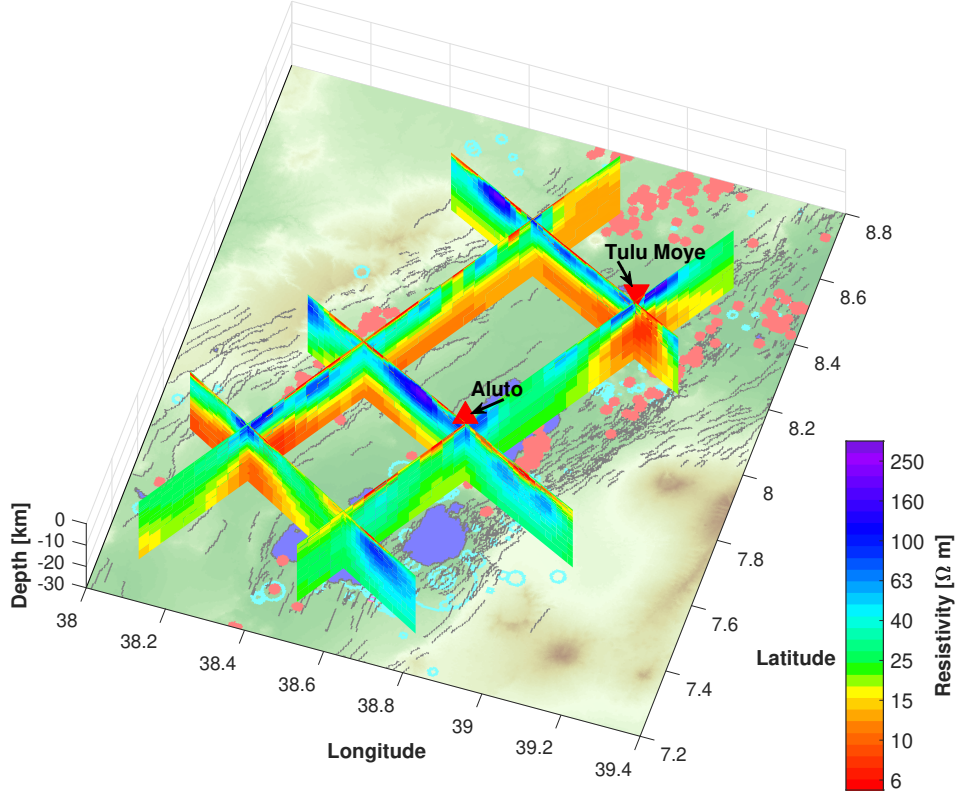


**Figure 6.** Profile slices through the preferred 3-D inversion model. The topographic map and position of lakes (blue areas) from Fig. 2 is displayed for orientation. Triangles indicate the position of Aluto volcano and Tulu Moye prospect at the surface.

ber of degrees of freedom in 3-D modelling. Additionally, the 2-D inversion is more robust to the choice of starting model. For the 3-D inversion, we chose a background of 25  $\Omega\text{m}$  derived from averaging all apparent resistivity values in the array because it significantly improved convergence and data fit.

#### 4.5 Estimation of Melt Content in the CMER

Electrical conductivity is sensitive to the melt content of the subsurface, and conductivity models derived from MT data have often been used to deduce a range of possible values in the crust and mantle (e.g., Rippe et al., 2013; Johnson et al., 2015; Comeau et al., 2015). To estimate the amount of melt present in the middle to lower crust under the CMER from the electrical resistivity model presented here, it is necessary to make some petrological assumptions to give constraints on the other parameters that influence bulk conductivity. Those describe the physical conditions in the lower crust (temperature and pressure), the melt composition (amount of silicate, free ions and water) and the mixing model (representing the geometry of melt in the rock matrix). For our estimation, the pressure ( $P$ ) follows a simple hydrostatic depth gradient ( $P = \rho g d$ , with  $g$  - acceleration of gravity,  $d$  - depth and  $\rho$  - density). We assume a homogeneous crustal density of  $\rho = 2800 \text{ kg/m}^3$  (Cornwell et al., 2006). The temperature ( $T$ ) is assumed to be depth independent at  $1190^\circ\text{C}$  (Iddon, 2020). For the composition of the melt we assume a predominantly mafic content ( $\text{SiO}_2 = 47.8 \text{ wt\%}$ , a sodium content of  $\text{Na}_2\text{O} 3.5 \text{ wt\%}$  based on Iddon and Edmonds (2020)). Silicic melt conductivity has been studied with laboratory experiments by e.g. Gaillard (2004); Guo et al. (2016). Computations of melt

electrical conductivity were performed with SIGMELTS, a well-used and comprehensive compendium of laboratory work presented by Pommier and Le-Trong (2011). We estimated the melt conductivity at depth levels from 4 to 38 km, which correspond to areas in our model that contain conductive anomalies associated with melt. For the shallower model parts, other mechanisms for enhancing electrical conductivity such as the presence of hydrothermal fluids play a bigger role and are not considered here. The hydrostatic pressure increases with depth, and we varied the water content from 0.9 to 1.4 wt% to estimate a range of possible melt conductivities, as the water content at depth is less well constrained by additional data and geological observations. Nevertheless, we derived only a relatively narrow range for the melt conductivity of 2.4 S/m (for shallower depths and dryer rocks) to 2.7 S/m (for deeper levels and higher water content).

With these estimates of melt conductivities, we can now examine the bulk conductivity of a melt-rock mix. We used different mixing models to explore the range of melt content that can be explained by our model's conductivities and ultimately chose the upper Hashin-Shtrikman bound (Hashin & Shtrikman, 1962), because this mixing model is appropriate for well-connected melts as expected in the CMER and also defines a more conservative estimate for the amount of melt necessary to explain enhanced electrical conductivity. The assumed conductivity of the non-melt component, the rock matrix, was set to 0.001 S/m. With these assumptions it is possible to estimate the relative melt content in each cell in our model and hence melt volumes in certain depth layers from the bulk conductivity inferred from MT. Note that the melt content derived this way can only reflect an average per model cell (with a 2x2 km horizontal discretization). Figure 7 shows the results of our melt content estimates at different depth levels. In the upper crust above 10 km depth, only a few areas indicate the presence of more than 4% melt, with the most prominent melt occurrence related to the Bora-Tulu-Moye volcanic field in the north-east. In the middle to lower crust below 15 km depth, melt content of > 4% becomes more pervasive, but is still limited to the area below the rift valley and does not extend laterally beyond the northern border fault or closer than  $\approx 50$  km to the southern border fault. These melt amounts are based on the MT inversion model and are therefore affected by low lateral resolution at these depths and increased smoothing due to the regularization in the inversion process. Therefore, our values are likely to be underestimates. As noted in section 4.3, we are unable to distinguish explicitly more pervasive, lower melt fractions from more concentrated higher fractions in the lower crust, although we expect the total melt content in each layer to be robust to regularization issues (Johnson et al., 2015).

## 5 Discussion

### 5.1 Comparison with Results from Seismic Studies in the CMER

In addition to deep electromagnetic sounding, seismic data have been widely used to investigate the interior of the earth. In general, the presence of melt will slow down, e.g. teleseismic waves, travelling from global earthquake locations through crust and mantle, which can be detected in an array of receivers. The EARS has been studied extensively in the past decades using seismic data from different seismic data collection campaigns, that recorded local events, teleseismic earthquakes, ambient noise and the signal from controlled sources to image the velocity distributions and ratios, Moho depth and seismic anisotropy in the crust and upper mantle (e.g., Kendall et al., 2006; Keir et al., 2006; Bastow et al., 2008; Keranen et al., 2009; Hammond et al., 2010). Many of these studies have presented evidence for the presence of melt at different depth levels in the EARS. For example, in the seismic anisotropy study of Kendall et al. (2005), the station at Butajira (8.1  $^{\circ}$ N, 38.38  $^{\circ}$ E, close to MT site LMT001) had a very large time delay (3.12 s) between the two shear wave modes, one of the highest in the world. In general, the largest amount of shear wave splitting occurs beneath the western rift flank (Kendall et al., 2005; Hammond et al., 2010). In this setting, seismic anisotropy was interpreted

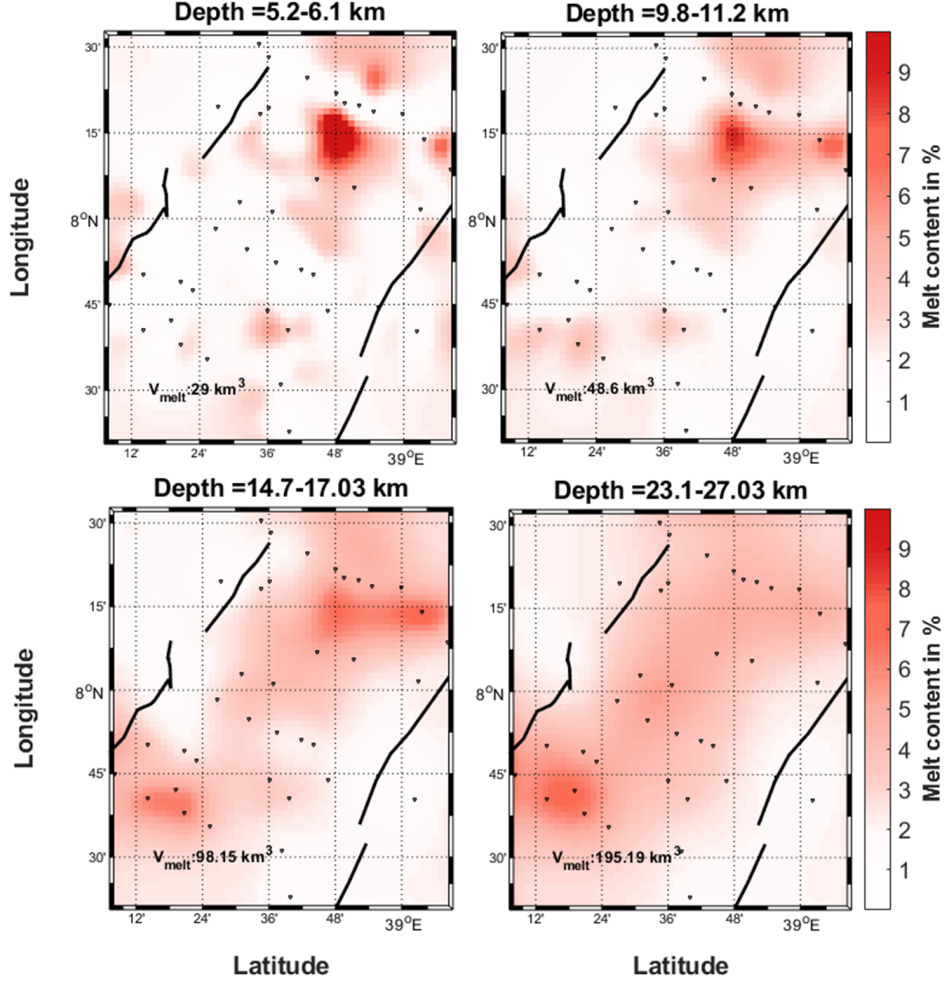


**Figure 7.** Melt content at different depth levels derived from the electrical conductivity model. The depth ranges correspond to the vertical discretization of the MT model. The volume indicated is the amount of melt in the respective depth layer. In the lower crust, melt is pervasive throughout the CMER, while at upper crustal levels there are more focused centres.

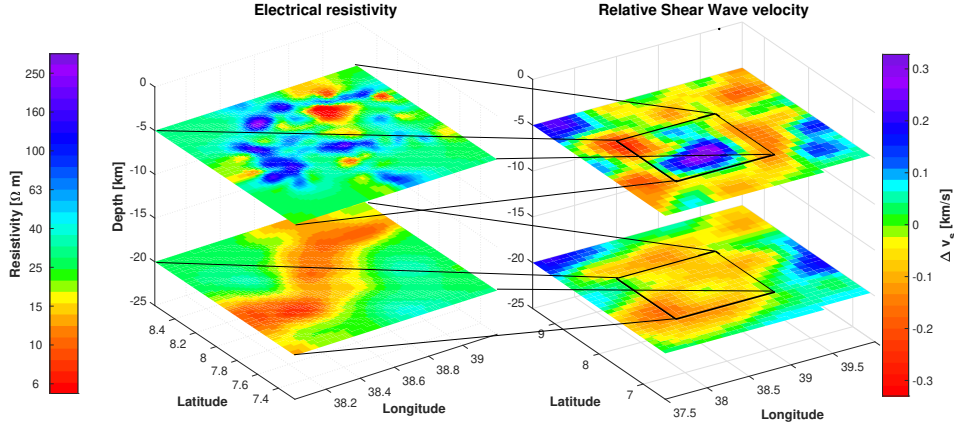


**Figure 8.** Comparison of electrical resistivity (left) and relative shear wave velocity (right) in the CMER, shown at depths of 5 and 20 km. The ambient noise shear wave velocity model is from Chambers et al. (2019) and displayed as deviation from the mean value per depth layer. In the CMER (7-8.5° N and 38-39° E) there is a clear change from relatively high shear wave velocities in the upper 10 km, which could be indicative of cooled intrusive bodies, to significantly slower velocities from 20 km down, suggesting increased melt content.

to be melt-induced, and the large delay thus indicates substantial quantities of melt that are focussed into narrow zones in the crust and mantle. Additionally, Stuart et al. (2006) found a very high crustal seismic velocity ratio  $V_p/V_s$  of 2.06 at Butajira that can only be explained by the presence of partial melt in the lower crust.

In the following we describe how the joint interpretation of seismic shear wave velocity models and the electrical conductivity model derived from our MT data can identify different zones of melt storage below the CMER.

Chambers et al. (2019) and Chambers et al. (2021) applied ambient noise tomography to derive shear wave velocity models of Afar and the MER. One of their main conclusions is that pervasive partial melt and focused upwelling can be found below the MER. In the CMER, two features in their shear wave model stand out (see Figure 8): an upper crustal fast zone at 5 km depth below the centre of the CMER, and a middle-lower crust slow zone encompassing the whole CMER at 20 km depth. These are co-located with the resistive area below Aluto volcano and the deeper rift-parallel elongated conductor in our MT inversion model, respectively.

Under Aluto volcano, the faster velocities in the shear wave model and the higher resistivities both point towards the presence of cooled igneous material in the upper crust. This is also in agreement with the higher Bouguer gravity anomalies in the same area (Mahatsente et al., 1999; Cornwell et al., 2010). Hübner et al. (2018) associated high Bouguer anomalies with the mid-crustal resistive bodies under Aluto.

At mid-crustal depths of about 20 km, the large zone of enhanced conductivity as presented in the previous section and slower S-wave velocities in the model of Chambers et al. (2019) and Chambers et al. (2021) below the CMER are both consistent with the presence of partial melt. The difference in lateral extent between the shear wave and resistivity models can be explained by the different resolution of the seismic velocity and MT conductivity models. The resolution of both methods depends on the spacing between measurement sites and can improve with more data points, but especially for the MT method there is an additional inherent dependence on the actual conductivity dis-

tribution in the model. In our case, the sensitivity of the MT data to lateral contrasts in the CMER is greater than that of the seismic data due to denser MT data sampling. In the seismic model, the phase velocities inverted for S-wave speed were an average along the ray path between seismic stations, and resolution depends on the intersection between crossing paths. Therefore, the resistivity model has better resolution and is imaging smaller and more extreme anomalies than the seismic model in the CMER. Chambers et al. (2021) also model radial anisotropy (the velocity difference between the two shear wave modes) over the region, and find that  $V_{SH} > V_{SV}$  in the CMER, consistent with a horizontally layered medium. Although the decrease in shear wave speed within the rift is higher in the 16-30 km depth range, anisotropy is greater ( $\sim 5\%$ ) at 5-15 km depths, interpreted as 2-4 % melt in thin sills (i.e. laterally connected), alternating with continental crust. (Johnson et al., 2015) showed that a conductive body in a regularized (2-D) model of MT data could instead be represented by a sill-like model fitting the data equally well.

## 5.2 Melt Storage and Connectivity in the Lower Crust

From the seismic and MT imaging methods presented we conclude that there is connectivity of melt in the lower crust and more discrete localization of melt in the upper crust. The question remains how melt is transported through the crust to the different volcanic centres. In Afar, dyke intrusion was not only observed during the past years but can also be inferred from conductivity models derived from MT data (Johnson et al., 2015). From our conductivity model of the CMER, only a few vertical connections between the deeper magma storage and the surface can be inferred, but others could be missed because of the limited resolution due to wider station spacing along, compared to across, the rift. Samrock et al. (2021) infer from their much higher resolution MT study of Aluto volcano that there is a narrow conductive ( $\sim 20 \Omega\text{m}$  resistivity) feature that could provide a pathway to feed the upper magmatic and hydrothermal system from a deeper level. The relatively small conductivity contrast and narrow width are beyond the resolution of our study, but the observation is again that there is no prominent conductive feature that could be interpreted as a magma chamber with large volumes of connected melt under the central volcano Aluto. From their local shear wave splitting study of Aluto, Nowacki et al. (2018) interpret a magma mush zone below 9 km depth, where there is a modest resistivity increase in the MT model of Samrock et al. (2021). Samrock et al. (2021) also image a much more conductive and wider connection under Tulu Moye volcano (probably related to their higher station density), and the position of their deep conductive feature C4 finds a good correspondence in our model. Our mid-crustal conductor lies about 20 km to the East of Tulu Moye (beyond the extent of their model) but connects laterally to it.

Other methods have also been used to address the storage of melt in the lower crust in the rift. Temtime et al. (2020) show a schematic model below the NMER with an extensive, connected mush zone in the lower crust using radar interferometry to study the surface deformation. This zone of melt storage only locally connects to volcanic centres at the surface, with dykes feeding laterally into Fentale volcano in the NMER. In contrast, Iddon and Edmonds (2020) developed a model of more localised melt in the lower crust beneath magmatic centres based on the geochemistry ( $\text{CO}_2$ ) of melt inclusions. However, we cannot distinguish explicitly more pervasive, lower melt fractions from more concentrated higher fractions in the lower crust (e.g. beneath the magmatic centres) due to limited lateral resolution (see section 4.3). Similar issues apply to interpretations of seismic data. However, there is broad agreement from a variety of methodologies for melt focussing at magmatic centres.

## 6 Conclusions

We have collected and analysed broadband and long-period magnetotelluric data collected in the Central Main Ethiopian Rift. A 3D model of electrical resistivity for the upper 35 km of the crust has been derived using an inverse modelling technique. The model contains relatively resistive features in the upper 7 km, most prominently under Aluto volcano and along the entire SE border of the rift valley. We associate higher resistivities with cooled igneous material. There are notable conductive anomalies in the upper crust around the Tulu Moya volcanic region which connect to a deeper conductive zone. Below 15 km depth, the model is dominated by a large conductive feature abutting the western boundary of the rift. We have interpreted the model below 4 km in terms of melt content and found that melt is pervasive ( $> 4\%$ ) in mid to lower crustal levels with only vertical pathways to the shallower crust. The presence of a resistor below Aluto volcano and the large deeper conductor find correspondence in features from a seismic shear wave velocity model derived by Chambers et al. (2019) that imaged a lower velocity zone at 5 km depth and a large low velocity area at around 20 km depth. Our results lend further weight to previous concepts of horizontal melt storage in the mid-lower crust below the MER, which is then focussed into narrow sub-vertical channels beneath the volcanic centers.

## Acknowledgments

This research was funded by NERC under grant number NE/L013932/1 as part of Rift Volcanism: Past, Present and Future (RiftVolc). RiftVolc included British Geological Survey, the Universities of Edinburgh, Bristol, Oxford, Cambridge, Southampton and Leeds, Addis Ababa University (AAU) and the Geological Survey of Ethiopia studying past and current volcanism and volcanic hazards in the central Main Ethiopian Rift. We benefited greatly from discussions with colleagues at these institutions. Emma Chambers provided a digital copy of the shear wave model of Chambers et al. (2019) that enabled a detailed comparison with our resistivity model. Special thanks go to the staff at the Institute for Geophysics, Space Science and Astronomy, AAU for logistic support, drivers and field crews, enabling successful field campaigns. Sam Engwell, Fiona Iddon, Neeraj Shah, Dagim Yoseph, Aklilu Bossa and the drivers from AAU are thanked for their in-field assistance. Dublin Institute of Advanced Studies and the NERC Geophysical Equipment Facility loaned instrumentation. We thank Reykjavik Geothermal for allowing us to use MT data from two stations of their Tulu Moya prospect. The authors of ModEM are thanked for making their code available to users. Naser Meqbel is thanked for providing his visualization and data manipulation software 3Dgrid. This work has made use of the resources provided by the Edinburgh Compute and Data Facility (ECDF) (<http://www.ecdf.ed.ac.uk/>). The MT data presented in this study are available openly on the National Geoscience Data Centre (Hübert & Whaler, 2020).

## References

- Agostini, A., Bonini, M., Corti, G., Sani, F., & Mazzarini, F. (2011). Fault architecture in the Main Ethiopian Rift and comparison with experimental models: Implications for rift evolution and Nubia-Somalia kinematics. *Earth and Planetary Science Letters*, 301(3-4), 479–492. doi: 10.1016/j.epsl.2010.11.024
- Bastow, I. D., Nyblade, A. A., Stuart, G. W., Rooney, T. O., & Benoit, M. H. (2008, DEC 18). Upper mantle seismic structure beneath the Ethiopian hot spot: Rifting at the edge of the African low-velocity anomaly. *GEOCHEMISTRY GEOPHYSICS GEOSYSTEMS*, 9. doi: {10.1029/2008GC002107}
- Caldwell, T. G., Bibby, H. M., & Brown, C. (2004). The magnetotelluric phase tensor. *Geophysical Journal International*, 158(2), 457–469. doi: 10.1111/j.1365-246X.2004.02281.x
- Cashman, K. V., Sparks, R. S. J., & Blundy, J. D. (2017, MAR 24). VOLCANOL-

- OGY Vertically extensive and unstable magmatic systems: A unified view of igneous processes. *SCIENCE*, 355(6331). doi: {10.1126/science.aag3055}
- Chambers, E. L., Harmon, N., Keir, D., & Rychert, C. A. (2019, APR). Using Ambient Noise to Image the Northern East African Rift. *GEO-CHEMISTRY GEOPHYSICS GEOSYSTEMS*, 20(4), 2091-2109. doi: {10.1029/2018GC008129}
- Chambers, E. L., Harmon, N., Rychert, C. A., & Keir, D. (2021). Variations in melt emplacement beneath the northern east african rift from radial anisotropy. *Earth and Planetary Science Letters*, 573, 117150. doi: https://doi.org/10.1016/j.epsl.2021.117150
- Chorowicz, J. (2005, OCT). The East African rift system. *JOURNAL OF AFRICAN EARTH SCIENCES*, 43(1-3), 379-410. doi: {10.1016/j.jafrearsci.2005.07.019}
- Comeau, M. J., Unsworth, M. J., Ticona, F., & Sunagua, M. (2015). Magnetotelluric images of magma distribution beneath Volcano Uturuncu, Bolivia: Implications for magma dynamics. *Geology*, 43(3), 243-246. doi: 10.1130/G36258.1
- Cornwell, D. G., Mackenzie, G. D., England, R. W., Maguire, P., Asfaw, L., & Oluma, B. (2006). Northern Main Ethiopian Rift crustal structure from new high-precision gravity data. *Geological Society, London, Special Publications*, 259(1), 307-321. doi: 10.1144/GSL.SP.2006.259.01.23
- Cornwell, D. G., Maguire, P. K. H., England, R. W., & Stuart, G. W. (2010, JAN 9). Imaging detailed crustal structure and magmatic intrusion across the Ethiopian Rift using a dense linear broadband array. *GEOCHEMISTRY GEOPHYSICS GEOSYSTEMS*, 11. doi: {10.1029/2009GC002637}
- Corti, G. (2009). Continental rift evolution: From rift initiation to incipient breakup in the Main Ethiopian Rift, East Africa. *Earth-Science Reviews*, 96(1-2), 1-53. doi: 10.1016/j.earscirev.2009.06.005
- Corti, G., Molin, P., Sembroni, A., Bastow, I. D., & Keir, D. (2018). Control of pre-rift lithospheric structure on the architecture and evolution of continental rifts: Insights from the main ethiopian rift, east africa. *Tectonics*, 37(2), 477-496. doi: 10.1002/2017TC004799
- Ebinger, C. J., & Casey, M. (2001). Continental breakup in magmatic provinces: An Ethiopian example. *Geology*, 29(6), 527-530. doi: 10.1130/0091-7613(2001)029<0527:CBIMPA>2.0.CO;2
- Egbert, G. D. (1997). Robust multiple-station magnetotelluric data processing. *Geophysical Journal International*, 130(2), 475-496. doi: 10.1111/j.1365-246X.1997.tb05663.x
- Fontijn, K., McNamara, K., Tadesse, A. Z., Pyle, D. M., Dessalegn, F., Hutchison, W., ... Yirgu, G. (2018). Contrasting styles of post-caldera volcanism along the main ethiopian rift: Implications for contemporary volcanic hazards. *Journal of Volcanology and Geothermal Research*, -. doi: https://doi.org/10.1016/j.jvolgeores.2018.02.001
- Gaillard, F. (2004). Laboratory measurements of electrical conductivity of hydrous and dry silicic melts under pressure. *Earth and Planetary Science Letters*, 218(1-2), 215-228. doi: 10.1016/S0012-821X(03)00639-3
- Greenfield, T., Keir, D., Kendall, J.-M., & Ayele, A. (2019a, NOV 15). Low-frequency earthquakes beneath Tullu Moya volcano, Ethiopia, reveal fluid pulses from shallow magma chamber. *EARTH AND PLANETARY SCIENCE LETTERS*, 526. doi: {10.1016/j.epsl.2019.115782}
- Greenfield, T., Keir, D., Kendall, J.-M., & Ayele, A. (2019b, FEB). Seismicity of the Bora-Tullu Moya Volcanic Field, 2016-2017. *GEOCHEMISTRY GEOPHYSICS GEOSYSTEMS*, 20(2), 548-570. doi: {10.1029/2018GC007648}
- Guo, X., Zhang, L., Behrens, H., & Ni, H. (2016, JAN 1). Probing the status of felsic magma reservoirs: Constraints from the P-T-H<sub>2</sub>O dependences of electrical conductivity of rhyolitic melt. *EARTH AND PLANETARY SCIENCE*

- LETTERS*, 433, 54-62. doi: {10.1016/j.epsl.2015.10.036}
- Hammond, J. O. S., Kendall, J.-M., Angus, D., & Wookey, J. (2010). Interpreting spatial variations in anisotropy: insights into the Main Ethiopian Rift from SKS waveform modelling. *Geophysical Journal International*, 181(3), 1701-1712. doi: <https://doi.org/10.1111/j.1365-246X.2010.04587.x>
- Hashin, Z., & Shtrikman, S. (1962). A variational approach to theory of effective magnetic permeability of multiphase materials. *Journal of applied physics*, 33(10), 3125-3131. doi: {10.1063/1.1728579}
- Hübert, J., & Whaler, K. (2020). *Magnetotelluric and transient electromagnetic data from the main ethiopian rift. british geological survey. (dataset)* (Tech. Rep.). National Geoscience Data Centre, British Geological Survey. doi: <https://doi.org/10.5285/2fb02ed4-5f50-4c14-aeec-27ee13aafc38>
- Hübert, J., Whaler, K., & Fisseha, S. (2018, JUL). The Electrical Structure of the Central Main Ethiopian Rift as Imaged by Magnetotellurics: Implications for Magma Storage and Pathways. *JOURNAL OF GEOPHYSICAL RESEARCH-SOLID EARTH*, 123(7), 6019-6032. doi: {10.1029/2017JB015160}
- Iddon, F. E. (2020). *Examining the past to prepare for the future: Quaternary magma storage in the main ethiopian rift and implications for volcanic hazard and resource potential*. (Doctoral dissertation, University of Cambridge, Department of Earth Sciences). doi: <https://doi.org/10.17863/CAM.49268>
- Iddon, F. E., & Edmonds, M. (2020). Volatile-Rich Magmas Distributed Through the Upper Crust in the Main Ethiopian Rift. *Geochemistry, Geophysics, Geosystems*, 21(6), e2019GC008904. (e2019GC008904 2019GC008904) doi: <https://doi.org/10.1029/2019GC008904>
- Johnson, N. E., Whaler, K. A., Hautot, S., Fisseha, S., Desissa, M., & Dawes, G. J. K. (2015). Magma imaged magnetotellurically beneath an active and an inactive magmatic segment in Afar, Ethiopia. *Geological Society, London, Special Publications*, 420, 105-125. doi: 10.1144/SP420.11
- Keir, D., Bastow, I. D., Whaler, K. A., Daly, E., Cornwell, D. G., & Hautot, S. (2009, JUN 18). Lower crustal earthquakes near the Ethiopian rift induced by magmatic processes. *GEOCHEMISTRY GEOPHYSICS GEOSYSTEMS*, 10. doi: {10.1029/2009GC002382}
- Keir, D., Stuart, G. W., Jackson, A., & Ayele, A. (2006). Local earthquake magnitude scale and seismicity rate for the Ethiopian rift. *Bulletin of the Seismological Society of America*, 96(6), 2221-2230. doi: 10.1785/0120060051
- Kelbert, A., Meqbel, N., Egbert, G. D., & Tandon, K. (2014, MAY). ModEM: A modular system for inversion of electromagnetic geophysical data. *COMPUTERS & GEOSCIENCES*, 66, 40-53. doi: {10.1016/j.cageo.2014.01.010}
- Kendall, J.-M., Pilidou, S., Keir, D., Bastow, I. D., Stuart, G. W., & Ayele, A. (2006). Mantle upwellings, melt migration and the rifting of Africa: Insights from seismic anisotropy. In G. Yirgu, C. J. Ebinger, & P. K. H. Maguire (Eds.), *The afar volcanic province within the east african rift system* (Vol. 259, p. 55-72). Geol. Soc. Spec. Publ.
- Kendall, J.-M., Stuart, G., Ebinger, C., Bastow, I., & Keir, D. (2005, JAN 13). Magma-assisted rifting in Ethiopia. *NATURE*, 433(7022), 146-148. doi: {10.1038/nature03161}
- Keranen, K. M., & Klemperer, S. L. (2008, JAN 15). Discontinuous and diachronous evolution of the Main Ethiopian Rift: Implications for development of continental rifts. *EARTH AND PLANETARY SCIENCE LETTERS*, 265(1-2), 96-111. doi: {10.1016/j.epsl.2007.09.038}
- Keranen, K. M., Klemperer, S. L., Julia, J., Lawrence, J. F., & Nyblade, A. A. (2009, MAY 8). Low lower crustal velocity across Ethiopia: Is the Main Ethiopian Rift a narrow rift in a hot craton? *GEOCHEMISTRY GEOPHYSICS GEOSYSTEMS*, 10. doi: {10.1029/2008GC002293}
- Lavayssiere, A., Rychert, C., Harmon, N., Keir, D., Hammond, J. O. S., Kendall,

- J.-M., ... Leroy, S. (2018). Imaging lithospheric discontinuities beneath the northern east african rift using s-to-p receiver functions. *Geochemistry, Geophysics, Geosystems*, 19(10), 4048-4062. doi: <https://doi.org/10.1029/2018GC007463>
- Maguire, P. K. H., Keller, G. R., Klemperer, S. L., MacKenzie, G. D., Keranen, K., Harder, S., ... Amha, M. (2006). Crustal structure of the northern Main Ethiopian Rift from the EAGLE controlled-source survey; a snapshot of incipient lithospheric break-up. In Yirgu, G and Ebinger, CJ and Maguire, PKH (Ed.), *AFAR VOLCANIC PROVINCE WITHIN THE EAST AFRICAN RIFT SYSTEM* (Vol. 259, p. 269+). (International Conference on East African Rift Systems - Geodynamics, Resources and Environment, Addis Ababa, ETHIOPIA, JUN, 2004) doi: {10.1144/GSL.SP.2006.259.01.21}
- Mahatsente, R., Jentzsch, G., & Jahr, T. (1999). Crustal structure of the Main Ethiopian Rift from gravity data: 3-dimensional modeling. *Tectonophysics*, 313(4), 363–382. doi: 10.1016/S0040-1951(99)00213-9
- Mazzarini, F., Keir, D., & Isola, I. (2013). Spatial relationship between earthquakes and volcanic vents in the central-northern Main Ethiopian Rift. *Journal of Volcanology and Geothermal Research*, 262, 123–133. doi: 10.1016/j.jvolgeores.2013.05.007
- Nowacki, A., Wilks, M., Kendall, J. M., Biggs, J., & Ayele, A. (2018, MAY 1). Characterising hydrothermal fluid pathways beneath Aluto volcano, Main Ethiopian Rift, using shear wave splitting. *JOURNAL OF VOLCANOLOGY AND GEOTHERMAL RESEARCH*, 356, 331-341. doi: {10.1016/j.jvolgeores.2018.03.023}
- Pommier, A., & Le-Trong, E. (2011, SEP). “SIGMELTS”: A web portal for electrical conductivity calculations in geosciences. *COMPUTERS & GEOSCIENCES*, 37(9), 1450-1459. doi: {10.1016/j.cageo.2011.01.002}
- Rippe, D., Unsworth, M. J., & Currie, C. A. (2013, OCT). Magnetotelluric constraints on the fluid content in the upper mantle beneath the southern Canadian Cordillera: Implications for rheology. *JOURNAL OF GEOPHYSICAL RESEARCH-SOLID EARTH*, 118(10), 5601-5624. doi: 10.1002/jgrb.50255
- Robertson, K., Thiel, S., & Meqbel, N. (2020, JAN 7). Quality over quantity: on workflow and model space exploration of 3D inversion of MT data. *EARTH PLANETS AND SPACE*, 72(1). doi: {10.1186/s40623-019-1125-4}
- Rooney, T. (2010). Geochemical evidence of lithospheric thinning in the southern Main Ethiopian Rift. *Lithos*, 117(1-4), 33–48. doi: 10.1016/j.lithos.2010.02.002
- Rooney, T. (2020, MAY). The Cenozoic magmatism of East Africa: Part V - Magma sources and processes in the East African Rift. *LITHOS*, 360. doi: {10.1016/j.lithos.2019.105296}
- Rooney, T., Furman, T., Bastow, I., Ayalew, D., & Yirgu, G. (2007). Lithospheric modification during crustal extension in the Main Ethiopian Rift. *Journal of Geophysical Research: Solid Earth*, 112(10). doi: 10.1029/2006JB004916
- Samrock, F., Grayver, A. V., Bachmann, O., Özge Karakas, & Saar, M. O. (2021). Integrated magnetotelluric and petrological analysis of felsic magma reservoirs: Insights from Ethiopian rift volcanoes. *Earth and Planetary Science Letters*, 559, 116765. doi: <https://doi.org/10.1016/j.epsl.2021.116765>
- Samrock, F., Grayver, A. V., Eysteinnsson, H., & Saar, M. O. (2018, DEC 16). Magnetotelluric Image of Transcrustal Magmatic System Beneath the Tulu Moyo Geothermal Prospect in the Ethiopian Rift. *GEOPHYSICAL RESEARCH LETTERS*, 45(23), 12847-12855. doi: {10.1029/2018GL080333}
- Samrock, F., Kuvshinov, A., Bakker, J., Jackson, A., & Fisseha, S. (2015). 3-D analysis and interpretation of magnetotelluric data from the Aluto-Langano geothermal field, Ethiopia. *Geophysical Journal International*, 202(3), 1923–1948. doi: 10.1093/gji/ggv270

- Smirnov, M. Y. (2003). Magnetotelluric data processing with a robust statistical procedure having a high breakdown point. *Geophysical Journal International*, 152(1), 1–7. doi: 10.1046/j.1365-246X.2003.01733.x
- Stuart, G. W., Bastow, I. D., & Ebinger, C. J. (2006). Crustal structure of the northern Main Ethiopian Rift from receiver function studies. In Yirgu, G and Ebinger, CJ and Maguire, PKH (Ed.), *AFAR VOLCANIC PROVINCE WITHIN THE EAST AFRICAN RIFT SYSTEM* (Vol. 259, p. 253+). (International Conference on East African Rift Systems - Geodynamics, Resources and Environment, Addis Ababa, ETHIOPIA, JUN, 2004) doi: {10.1144/GSL.SP.2006.259.01.20}
- Temtime, T., Biggs, J., Lewi, E., & Ayele, A. (2020, JUN). Evidence for Active Rhyolitic dike Intrusion in the Northern Main Ethiopian Rift from the 2015 Fentale Seismic Swarm. *GEOCHEMISTRY GEOPHYSICS GEOSYSTEMS*, 21(6). doi: {10.1029/2019GC008550}
- Wiese, H. (1962). Geomagnetische Tiefentellurik Teil II: die Streichrichtung der Untergrundstrukturen des elektrischen Widerstands, erschlossen aus geomagnetischen Variationen. *PAGEOPH*, 83-103.
- Wilks, M., Kendall, J.-M., Nowacki, A., Biggs, J., Wookey, J., Birhanu, Y., ... Bedada, T. (2017, JUN 15). Seismicity associated with magmatism, faulting and hydrothermal circulation at Aluto Volcano, Main Ethiopian Rift. *JOURNAL OF VOLCANOLOGY AND GEOTHERMAL RESEARCH*, 340, 52-67. doi: {10.1016/j.jvolgeores.2017.04.003}
- Woldegabriel, G., Aronson, J. L., & Walter, R. C. (1990). Geology, geochronology, and rift basin development in the central sector of the main ethiopia rift. *GSA Bulletin*, 102(4), 439. doi: 10.1130/0016-7606(1990)102<0439:GGARBD>2.3.CO;2